

**Magnetic correlations and structure in bixbyite across the spin-glass transition**Nikolaj Roth,<sup>1</sup> Feng Ye,<sup>2</sup> Andrew F. May,<sup>3</sup> Bryan C. Chakoumakos,<sup>2,\*</sup> and Bo Brummerstedt Iversen<sup>1,†</sup><sup>1</sup>*Center for Materials Crystallography (CMC), Department of Chemistry and Interdisciplinary Nanoscience Center (iNANO), Aarhus University, Langelandsgade 140, Aarhus 8000, Denmark*<sup>2</sup>*Neutron Scattering Division, Oak Ridge National Laboratory, Oak Ridge, Tennessee 37831, USA*<sup>3</sup>*Materials Science and Technology Division, Oak Ridge National Laboratory, Oak Ridge, Tennessee 37831, USA*

(Received 31 March 2019; revised manuscript received 6 July 2019; published 2 October 2019)

Magnetic frustration in atomically ordered crystals gives rise to a broad range of quantum phenomena. The mineral bixbyite,  $\text{Fe}_{2-x}\text{Mn}_x\text{O}_3$ , has magnetic frustration induced by atomic disorder. The end-members  $\text{Mn}_2\text{O}_3$  and  $\beta\text{-Fe}_2\text{O}_3$  both have magnetically ordered ground states, but the bixbyite crystal studied here, with a composition  $\text{Fe}_{1.12}\text{Mn}_{0.88}\text{O}_3$ , instead undergoes a spin-glass-like transition near 32 K. In this study, the magnetic correlations and atomic structure of bixbyite are followed across the spin-glass transition using powder and single-crystal neutron scattering. Refinement of Bragg intensities from neutron diffraction data allows precise determination of the average Fe and Mn concentration on the different crystallographic sites of the structure. No structural transitions occur in bixbyite upon cooling. Using the three-dimensional magnetic difference pair distribution function (3D-m $\Delta$ PDF), the magnetic correlations are resolved spatially and their temperature dependence determined. The results demonstrate that the spin-spin correlations are strong well above the glass transition temperature, consistent with the spin-glass nature of the magnetism in bixbyite.

DOI: [10.1103/PhysRevB.100.144404](https://doi.org/10.1103/PhysRevB.100.144404)**I. INTRODUCTION**

Magnetically disordered materials with short-range magnetic correlations are attracting strong interest due to their exotic properties. Examples of such materials are spin liquids [1,2], spin ices [3,4], spin glasses [5–7], multiferroics [8–10], and unconventional superconductors [11,12]. To understand such magnetic materials, determination of their magnetic correlations is essential, and this is typically done through neutron-scattering experiments. Magnetically ordered materials produce sharp Bragg peaks in a neutron-scattering experiment, which can be analyzed using conventional crystallographic methods to obtain the magnetic structure. However, magnetically disordered materials only give rise to diffuse neutron scattering, which requires different analysis methods.

Several different approaches have been used to understand short-range magnetic correlations. One is to calculate the diffuse scattering of a predetermined model for the system and compare it to the measured scattering data, e.g., Ref. [13]. This approach requires that accurate models of the magnetic interactions between the atoms are available, which can be challenging for complex systems. Another approach is the reverse Monte Carlo method, where a supercell model for the spins in the structure is developed, and the spin orientations are varied until the closest match to the measured scattering pattern is obtained. This method has been successful for determining magnetic correlations from both single-crystal and powder scattering data [14,15]. However, this method requires knowledge of the exact atomic arrangement in the

crystal to set up the modeling of the magnetic system. This makes it difficult to apply to structurally disordered systems or to systems where the atomic structure is unknown.

A different approach has been to transform the magnetic diffuse scattering into direct space, giving a more intuitive picture of the magnetic short-range correlations, which is particularly helpful in cases where the type of magnetic disorder or the atomic structure is unknown. This was first done using the magnetic pair distribution function (mPDF) analysis for powder neutron scattering [16,17]. Such analysis gives a one-dimensional representation of the pairwise magnetic correlations, both ordered and disordered. Recently, we generalized this method for single-crystal scattering, developing a three-dimensional magnetic difference pair distribution function (3D-m $\Delta$ PDF). This function provides a model-independent three-dimensional reconstruction of local magnetic correlations in real space [18]. A similar approach also has been used in the study of spin misalignment in ferromagnets, where Fourier transformation of small-angle neutron-scattering data provides two-dimensional information about spin misalignment on the nanometer scale [19,20]. In our previous paper where we introduced the 3D-m $\Delta$ PDF method, the diffuse scattering from bixbyite at 7 K was used as an example to show that it is feasible to measure the 3D-m $\Delta$ PDF experimentally. In this study we will give a more detailed analysis of the 3D-m $\Delta$ PDF of bixbyite to better understand the magnetic correlations at low temperatures and additionally, follow these correlations across the spin-glass transition.

Bixbyite  $(\text{Mn}^{+3}, \text{Fe}^{+3})_2\text{O}_3$  has the  $\beta\text{-Mn}_2\text{O}_3$  crystal structure (cubic,  $Ia\bar{3}$ ,  $a = 9.41 \text{ \AA}$ ) [21]. It contains two metal sites located on the  $24d$  and  $8b$  crystallographic positions. Both sites are approximately octahedrally coordinated to oxygen, the  $8b$  site having a small trigonal distortion and the  $24d$

\*chakoumakobc@ornl.gov

†bo@chem.au.dk

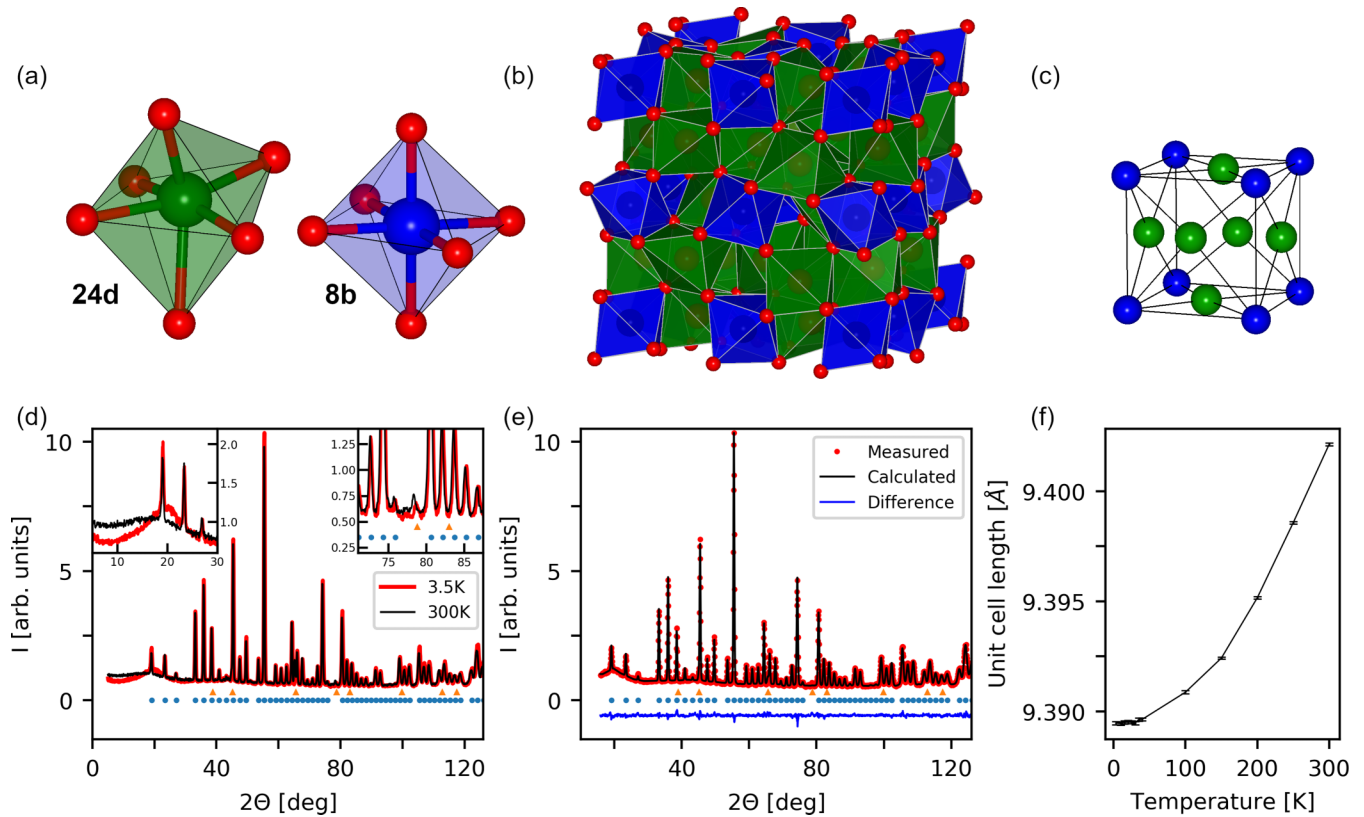


FIG. 1. Periodic structure of bixbyite. (a) The local geometry of the metal sites. Blue and green are the two metal sites and red is oxygen. (b) The unit cell of bixbyite. (c) Distorted fcc structure of metal sites only. (d) Neutron powder diffraction data at 3.5 and 300 K for bixbyite. Blue circles mark Bragg positions for bixbyite and orange triangles mark Bragg positions for the sample container (aluminum). The left inset shows the low-angle region with diffuse scattering, and the right inset shows a region with a visible peak from the sample container. (e) Refined nuclear model for the neutron diffraction data at 3.5 K. As can be seen, the fit also follows the broad diffuse peak at  $20^\circ$ . Here the diffuse scattering is fitted as part of the background and not as part of the structure itself. (f) Unit-cell parameter for bixbyite as a function of temperature.

site having a larger distortion, as shown in Figs. 1(a) and 1(b). The structure of the metal sites can be regarded as a face-centered cubic (fcc) structure, where the face-centered positions are slightly distorted, as seen in Fig. 1(c). Since  $\text{Fe}^{3+}$  and  $\text{Mn}^{3+}$  have a difference of only one electron, they have almost equal x-ray scattering factors, and the distribution of Fe and Mn on the two metal sites cannot be well determined from conventional x-ray diffraction experiments. It has been shown by Mössbauer spectroscopy that Fe prefers the higher symmetry  $8b$  site [22–24] and that with increasing the synthesis temperature, the distribution becomes more equal on the two sites [25]. Using neutron-scattering data we are here able to accurately determine the distribution of Mn and Fe on the two metal sites, as the neutron coherent cross sections for Mn and Fe are  $-3.7$  and  $9.5$  fm, respectively, giving a high contrast.

Compared with the pure end-members  $\text{Mn}_2\text{O}_3$  and  $\beta\text{-Fe}_2\text{O}_3$ , the solid solutions behave remarkably different. The nuclear structure for end-member  $\text{Mn}_2\text{O}_3$  is cubic above 308 K ( $\beta\text{-Mn}_2\text{O}_3$ ) and orthorhombic  $Pbca$  below. This structural transition is fully suppressed by addition of 9 mol % Fe. Magnetic transitions in  $\text{Mn}_2\text{O}_3$  occur at 80 and 25 K. The upper magnetic transition drops to  $\sim 35$  K beyond 9 mol % Fe content, and the lower transition disappears altogether beyond

1 mol % Fe [24]. The magnetic structure of low-temperature orthorhombic  $\text{Mn}_2\text{O}_3$  is ordered and has been solved both at 40 and 2 K from neutron diffraction data [26]. The pure  $\beta\text{-Fe}_2\text{O}_3$  has the cubic bixbyite structure. However, it is not as widely studied as the other  $\text{Fe}_2\text{O}_3$  polymorphs as it is metastable and will transform into hematite  $\alpha\text{-Fe}_2\text{O}_3$  at temperatures of 500 °C [27].  $\beta\text{-Fe}_2\text{O}_3$  has a magnetic transition to an antiferromagnetic state with a Néel temperature of 110–119 K. Based on magnetization measurements, heat-capacity measurements, and Mössbauer spectroscopy, this state was found to be ordered [28,29]. The ordered magnetic structures of both  $\text{Mn}_2\text{O}_3$  and  $\beta\text{-Fe}_2\text{O}_3$  are in contrast to the mixed bixbyite. We previously found that bixbyite of the composition  $\text{Fe}_{1.1}\text{Mn}_{0.9}\text{O}_3$  has a magnetic transition at 32 K to a glasslike state without long-range magnetic ordering [18]. Thus, the mixing of Mn and Fe in the bixbyite structure leads to a suppression of magnetic ordering.

We have previously reported physical property measurements of the bixbyite crystals used in the current study. These include time, temperature- and field-dependent DC magnetization, ac magnetic susceptibility, and specific heat-capacity measurements (see supporting information of [18]). These measurements all show behavior consistent with bixbyite undergoing a transition to a spin-glass state at approximately

$T^* = 32$  K. The data further show a negative Weiss temperature of  $\Theta = -336$  K, indicating that antiferromagnetic interactions are dominant in the high-temperature paramagnetic phase. The frustration ratio,  $|\Theta|/T^* = 10.3$ , demonstrates a significant amount of frustration in the sample. The magnetization shows a strong deviation from Curie-Weiss behavior below approximately 150 K. It would be expected that  $\text{Fe}^{3+}$  and  $\text{Mn}^{3+}$  ions octahedrally coordinated to O would have high-spin configurations with orbital moments quenched. This would result in magnetic moments of  $5.9\mu_B$  and  $4.9\mu_B$ , respectively, giving an expected average of  $5.5\mu_B$  per metal site. From fitting the Curie-Weiss law in the 200–380 K region, we previously obtained the average magnetic moment per site to be  $4.1(1)\mu_B$ , indicating that some degree of antiferromagnetic correlation was still present at high temperatures. Here we further investigate the spin-glass transition, the persistence of magnetic correlations above the freezing temperature, as well as the atomic structure in bixbyite.

## II. EXPERIMENTAL

Single-crystal elastic neutron scattering was measured at the CORELLI instrument at the Spallation Neutron Source at Oak Ridge National Laboratory [30,31]. A piece was cut from a large cubic crystal from the Thomas Range, Juab County, Utah, USA, and subsequently sanded down to a sphere to limit crystal shape effects in the scattering. The crystal was glued to the end of an aluminum pin which was wrapped in neutron absorbing Cd foil and mounted in a low-background closed-cycle refrigerator. Measurements were carried out at 7, 25, 50, 80, 160, 240, and 300 K. Bragg peaks were integrated using an instrument-specific script, corrected for absorption and merged using XPREP [32] to  $m$ -3 symmetry. The structure was refined using SHELXL [33] in space group  $Ia\bar{3}$ . Both metal sites were refined as a combination of Mn and Fe with the constraint that each site is fully occupied. The twin law  $[1,0,0;0,0,1,0,1,0]$  was used during refinement. The treatment of the diffuse scattering data to obtain a 3D-m $\Delta$ PDF is described in detail in [18].

Neutron powder diffraction data was measured at the HB-2A Neutron Powder Diffractometer at the Spallation Neutron Source at Oak Ridge National Laboratory. Several crystals, also from the Thomas Range, were ground to a fine powder. The sample was placed in a cryostat, and experiments were carried out with a neutron wavelength of  $1.5397(5)$  Å at temperatures of 3.5, 10, 15, 20, 25, 30, 35, 40, 100, 150, 200, 250, and 300 K. The data were fitted with a structural model using the Rietveld method as implemented in the FULLPROF software [34]. The structural model was the same as used for the single-crystal experiment described above. A small impurity of Al coming from the sample environment was also modeled.

## III. RESULTS

### A. Periodic average structure

From both the single-crystal and powder neutron diffraction data we obtain the distribution of Fe and Mn on the two metal sites. For the powder sample we find the occupancy of Mn on the  $24d$  site to be  $0.509(3)$  and on the  $8b$  site to be  $0.241(5)$ . From the single-crystal data we get Mn occupancies

of  $0.508(9)$  for the  $24d$  site and  $0.246(1)$  on the  $8b$  site. The Fe occupancies on these sites are 1 minus the Mn occupancies. This shows that the Fe favors the more symmetric  $8b$  site, which is in agreement with results obtained from Mössbauer spectroscopy [22–25]. From these occupancies the sample composition is then  $\text{Fe}_{1.12(1)}\text{Mn}_{0.88(1)}\text{O}_3$ . This is in agreement with our previous report of  $\text{Fe}_{1.1}\text{Mn}_{0.9}\text{O}_3$  measured on the same single-crystal sample used here [18]. It is notable that both samples have identical average structures within the standard deviations. The single crystals used for the powder sample as well as the single crystal used for measurements all came from the Thomas Range, Juab County, Utah, USA. This suggests that samples obtained from this area are similar with a composition of  $\text{Fe}_{1.12(1)}\text{Mn}_{0.88(1)}\text{O}_3$ . Bixbyite from the Thomas Range occurs in lithophysal gas cavities within rhyolitic volcanic rocks. It is not known at what point during the cooling of these lava flows that bixbyite crystallized, but the initial rhyolite flow temperatures are estimated to be around  $700^\circ\text{C}$  [35].

When cooling the samples, no structural transitions or transitions to ordered magnetic states are observed. In Fig. 1(d) the powder neutron diffraction data for 300 and 3.5 K are shown. The Bragg peaks almost overlap completely, but a small shift occurs as the unit cell contracts slightly upon cooling. Furthermore, the high-angle scattering is lowered slightly in the 300-K data as a consequence of the Debye-Waller factor. The unit-cell length changes continuously with temperature as shown in Fig. 1(f). The data at all temperatures is fitted with only a periodic nuclear structure and no long-range magnetic structure. The diffuse scattering in the data is then accounted for as part of the background. The fit for the 3.5-K dataset is shown in Fig. 1(e). A small Al impurity from the sample environment is also observed and refined, as shown by orange marks in Figs. 1(d) and 1(e). When looking closer at the 300- and 3.5-K dataset, two main differences can be seen. At low angles ( $10^\circ$ – $30^\circ$ ) the diffuse scattering has changed, indicating changes in the short-range magnetic correlations. This can be seen in the left inset in Fig. 1(d). At higher angles some of the weak peaks have shifted more than others. These are the stray Bragg peaks from the Al sample container, which has a larger contraction upon cooling than bixbyite. One example of this is shown in the right inset in Fig. 1(d), where the peak at  $78^\circ$  comes from the Al sample container.

### B. Magnetic correlations

A more detailed look at the magnetic diffuse scattering is obtained from the single-crystal data. In Figs. 2(a)–2(d) the  $HK0$  plane of the neutron scattering from bixbyite is shown at 7, 50, 80, and 240 K. As for the powder data, the only change with temperature is in the diffuse scattering. This is magnetic diffuse scattering as the intensity rapidly falls off at large momentum transfer because of the magnetic form-factor. The magnetic diffuse scattering is isolated from the nuclear scattering by subtracting the 300-K dataset and using the punch-and-fill method for Bragg peaks, as described in [18]. The isolated magnetic diffuse scattering for these temperatures is shown in Figs. 2(e)–2(h). At 7 K there is a strong magnetic diffuse signal which continuously weakens with increasing temperature and almost vanishes at 240 K. In

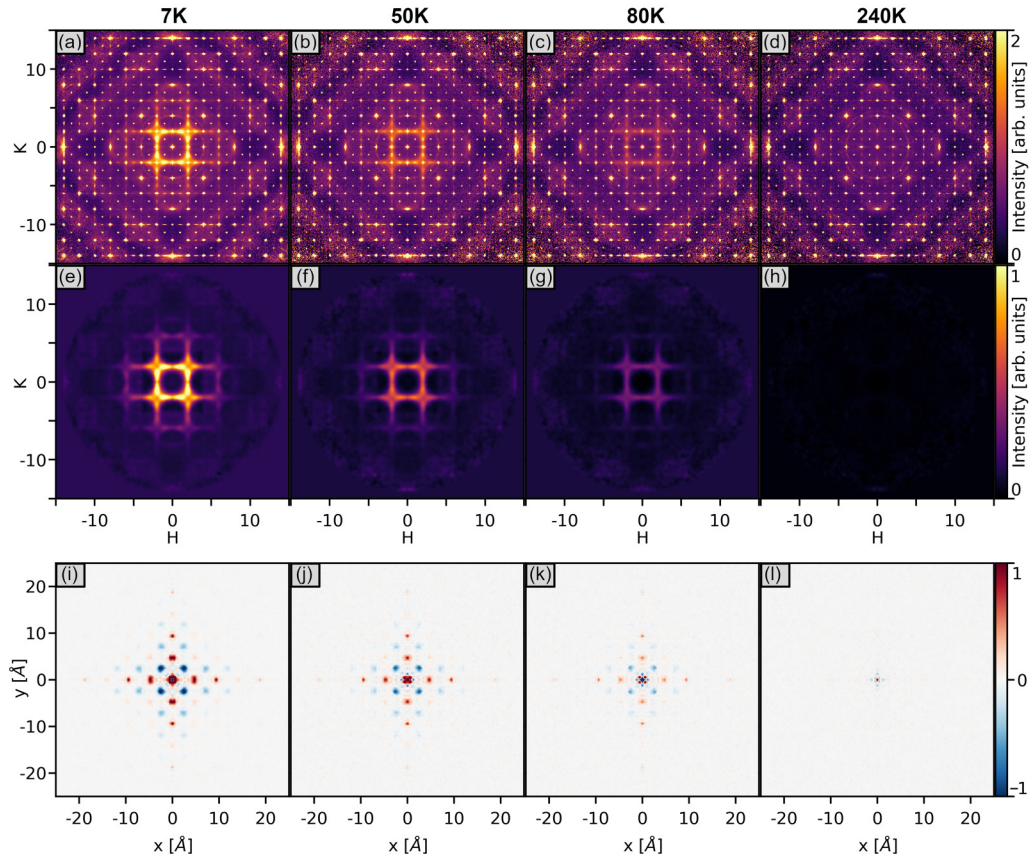


FIG. 2.  $HK0$  plane of the total elastic neutron scattering from bixbyite at (a) 7 K, (b) 50 K, (c) 80 K, and (d) 240 K.  $HK0$  plane of the isolated magnetic scattering at (e) 7 K, (f) 50 K, (g) 80 K, and (h) 240 K.  $z = 0$  plane of the 3D-m $\Delta$ PDF for (i) 7 K, (j) 50 K, (k) 80 K, and (l) 240 K.

the data reduction to obtain the diffuse scattering, the cross-correlation feature of the CORELLI instrument was used. This allows for the separation of the quasielastic scattering from the total scattering, which helps in eliminating phonon and other inelastic scattering contributions from the data. The CORELLI instrument's elastic resolution changes with the scattering vector, and the resolution is better for short scattering vectors than long. The scattering vector dependency of the energy resolution is discussed in [31], where they find the energy resolution to range from 0.4 to 2.5 meV for a collected dataset.

The magnetic diffuse scattering is analyzed using the three-dimensional magnetic difference pair distribution function (3D-m $\Delta$ PDF). This allows the local spin-spin correlations to be visualized in real-space coordinates, as in Figs. 2(i)–2(l). This function is defined as the inverse Fourier transform of the unpolarized magnetic diffuse neutron-scattering cross section [18]:

$$3\text{D-m}\Delta\text{PDF} = \mathcal{F}^{-1} \left[ \frac{d\sigma_{\text{Diffuse}}}{d\Omega} \right].$$

The function is related to the difference magnetization density of the sample,

$$\delta\mathbf{M}(\mathbf{r}) = \mathbf{M}(\mathbf{r}) - \mathbf{M}_{\text{periodic}}(\mathbf{r}),$$

where  $\mathbf{M}(\mathbf{r})$  is the total vector magnetization density, and  $\mathbf{M}_{\text{periodic}}(\mathbf{r})$  is the average periodic magnetization density. In the case where there is no periodic magnetic ordering, as is the case for bixbyite, the difference magnetization density is equal to the total magnetization density. The relation between the 3D-m $\Delta$ PDF and the magnetization density then becomes

$$3\text{D-m}\Delta\text{PDF} = \frac{r_0^2}{4\mu_B^2} \left\langle \mathbf{M} \bar{\otimes} \mathbf{M} - \frac{1}{\pi^4} (\mathbf{M} \bar{*} \boldsymbol{\Upsilon}) \otimes (\mathbf{M} \bar{*} \boldsymbol{\Upsilon}) \right\rangle,$$

where we defined the vector field cross-correlation operator as a combination of elementwise cross correlation and a dot product,

$$\mathbf{f} \bar{\otimes} \mathbf{g} \stackrel{\text{def}}{=} f_1 \otimes g_1 + f_2 \otimes g_2 + f_3 \otimes g_3,$$

where  $f_i$  and  $g_i$  are the vector components of  $\mathbf{f}$  and  $\mathbf{g}$ . Similarly, we have defined the vector field convolution operator  $\bar{*}$  from the scalar field convolution  $*$ . The smearing function modifying the magnetization density in the second term is given by

$$\boldsymbol{\Upsilon}(\mathbf{r}) = \begin{cases} \frac{\mathbf{r}}{|\mathbf{r}|^4}, & |\mathbf{r}| \neq 0 \\ 0, & |\mathbf{r}| = 0 \end{cases}.$$

The 3D-m $\Delta$ PDF contains information about the relative orientation of magnetic moments through the two terms in the

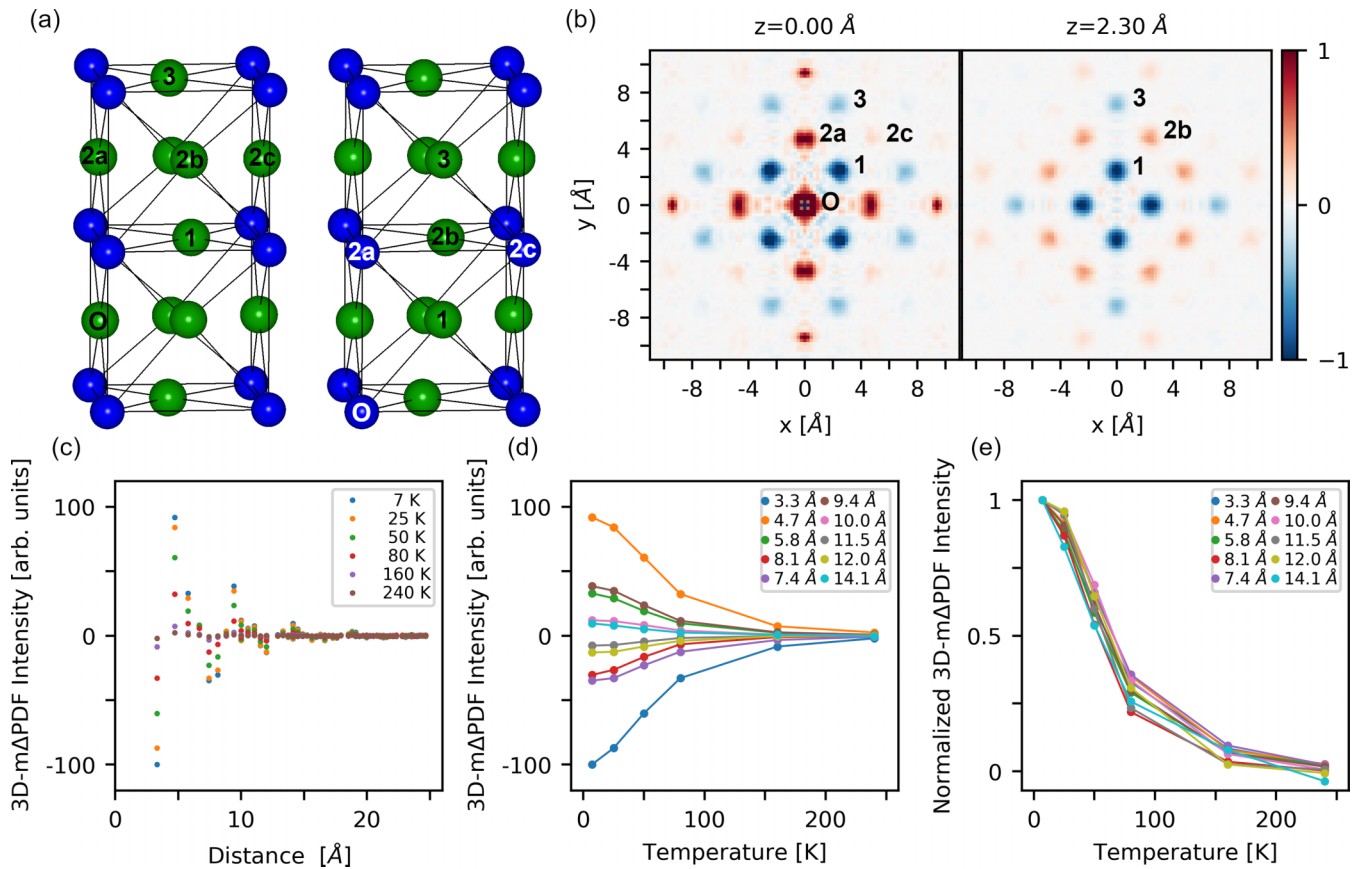


FIG. 3. (a) Structure of metal sites in bixbyite with numbers marking vectors starting at “O.” (b) Cuts through the 3D-m $\Delta$ PDF for  $z = 0$  and  $2.30 \text{ \AA}$ , with marked features corresponding to the vectors in (a). (c) Integrated peak amplitudes of the 3D-m $\Delta$ PDF as a function of distance for different temperatures. (d) The ten strongest 3D-m $\Delta$ PDF integrated peak amplitudes as a function of temperature. (e) Normalized peak amplitudes for the ten strongest 3D-m $\Delta$ PDF peaks as a function of temperature.

equation. The first term, which is the vector autocorrelation of the magnetization density, will give a positive peak for moments with an angle less than  $\pi/2$  (more parallel) and a negative peak for moments with an angle larger than  $\pi/2$  (more antiparallel). In the case where moments are perpendicular, this first term will give zero contribution. The second term will add lobes to the side of the peak generated by the first term. The main effect of this is to give the peaks a shape which is elongated along the direction of the moments and with lobes of opposite sign to the peak in directions perpendicular to the moments. In cases of particularly high symmetry, the lobes generated from different symmetry-equivalent orientations will average to an isotropic contribution and not be visible. This second term is also often weaker than the first term, unless the moments are almost perpendicular. This means that the sign of the 3D-m $\Delta$ PDF at the center of the peak shows whether the moments separating the vector will tend to align more parallel or antiparallel. A positive peak in the 3D-m $\Delta$ PDF indicates preference for moments to align in the same direction, and a negative peak indicates opposite alignment of magnetic moments [18].

Figures 2(i)–2(l) show the  $z = 0$  planes of the 3D-m $\Delta$ PDF for 7, 50, 80, and 240 K. Strong correlations, both positive and negative, are seen at 7 K. When increasing the temperature, these features decay in the same way as the magnetic

scattering in Figs. 2(e)–2(h). These correlations are observed up to a distance of around  $15 \text{ \AA}$ , as seen by the envelope of the extent of the peaks in the 3D-m $\Delta$ PDF. When looking closer at this envelope it seems that there could be some degree of anisotropy in the magnetic short-range order, as the correlations are visible to longer distances in some directions than others. As the features are strongest along the unit-cell axes of the crystal, it could suggest that the magnetic interactions are strongest along these directions. This ability to see the differing correlation lengths along different directions of the crystal would not be possible with the one-dimensional magnetic pair distribution function, where only the directionally averaged correlation length would be seen.

Cuts through the 3D-m $\Delta$ PDF for bixbyite at 7 K are shown in Fig. 3(b) together with the atomic structure in Fig. 3(a). Peaks in the 3D-m $\Delta$ PDF have been marked with numbers corresponding to the vectors in the structure, where the vectors in the structure start at the atom marked “O.” As the metal-site structure is close to fcc, the  $24\text{-}24d$  and  $8b\text{-}24d$  vectors are almost equal. Based on the broadness of the peaks in the 3D-m $\Delta$ PDF, the  $24d\text{-}24d$ ,  $8b\text{-}8b$ , and  $8b\text{-}24d$  correlations are therefore not directly distinguishable. The peak for the nearest-neighbor vector is marked “1” in the figure. As this is a negative peak, the nearest-neighbor sites tend to have magnetic moments aligned opposite to each other.

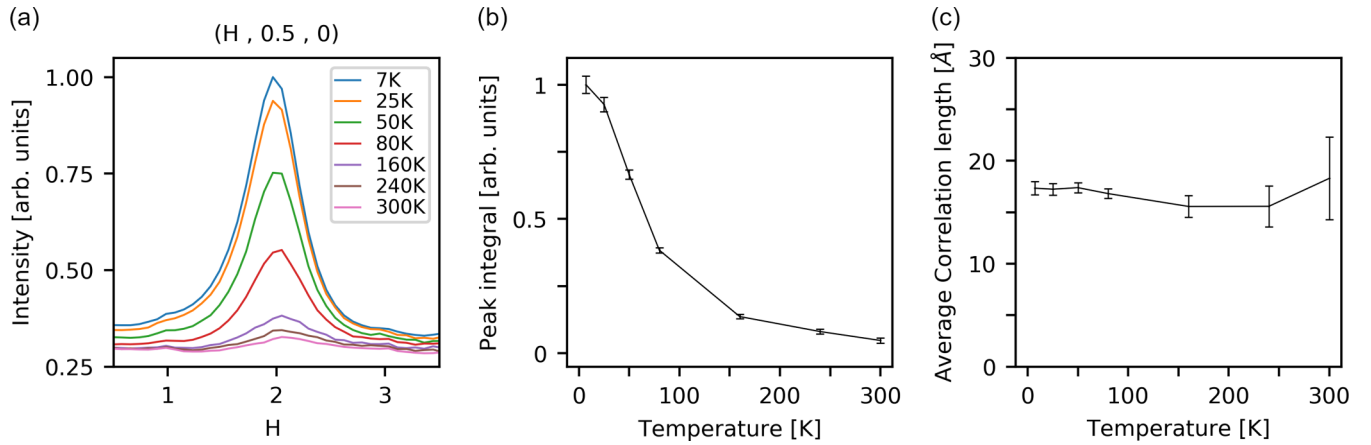


FIG. 4. (a) Diffuse scattering along the  $(H, 0.5, 0)$  line at around  $H = 2$ , chosen as there are no Bragg peaks there. (b) Peak integral of fitted Lorentzian function to the diffuse maxima. (c) Average correlation length found from the width of the diffuse maxima.

It is assumed that the interaction between the nearest-neighbor metal sites are mediated through the oxygen bridge between the two atoms. Further neighbors can then be grouped by the number of oxygen bridges needed to get from one metal site to the other. The second neighbor vectors, which require going through two oxygen bridges, are marked  $2a$ ,  $2b$ , and  $2c$  and show positive peaks in the 3D-m $\Delta$ PDF, indicating that the moments on the second neighbors tend to have alignment in the same direction. The third neighbor vector, marked 3, again shows a negative peak, indicating the preference for opposite alignment of spins separated by this vector. The correlation sign is alternating with the order of neighbors, extending to about 15 Å. Overall, the 3D-m $\Delta$ PDF for bixbyite clearly shows the disordered low-temperature state to be dominated by antiferromagnetic nearest-neighbor interactions.

As was seen in Figs. 2(i)–2(l), the features in the 3D-m $\Delta$ PDF decay at higher temperatures. To get a better understanding of this, the peak amplitudes of the 3D-m $\Delta$ PDF have been integrated, and they are shown as a function of distance in Fig. 3(c) for the different temperatures. The first five distances correspond to vectors of types 1,  $2a$ ,  $2b$ ,  $2c$ , and 3, respectively. It is seen that correlations exist up to around 15 Å in the low-temperature state, and that at high temperatures all magnetic correlations have almost vanished. The temperature dependence of the ten most intense peaks are shown in Fig. 3(d). All of them have a gradual decay, showing that the magnetic correlations of the spin-glass state are present over a wide temperature range. To compare the temperature dependence of the different peaks, the normalized peak amplitudes are shown in Fig. 3(e). All the peaks have almost the exact same temperature dependence. This suggests that the same type of correlations are present at all measured temperatures, whereby the average extent of the correlations are temperature independent, and that only the correlation amplitude changes with temperature.

That the average correlation length is independent of temperature is also found from a more conventional analysis of the total scattering data. From the inverse of the broadness of the diffuse features, the length scale of the local order can be estimated. We obtain this by fitting the diffuse max-

ima along the  $(H, 0.5, 0)$  line at around  $H = 2$  (as there are no Bragg peaks there) with a Lorentzian function,  $L(H) = c + \frac{S\gamma}{\pi [(H-H_0)^2 + \gamma^2]}$ , where  $c$  is a flat background term,  $S$  is the integrated amplitude of the peak,  $H_0$  is the center of the peak, and  $2\gamma$  is the FWHM. The average correlation length is then calculated as  $Average\ Correlation\ Length = a/\sqrt{FWHM^2 - FWHM_{inst}^2}$ , where  $a$  is the unit-cell length and  $FWHM_{inst}$  is the instrumental broadening, here estimated as the width of the close (400) Bragg peak, which is not affected by diffuse scattering. Figure 4(a) shows the scattering intensity along the  $(H, 0.5, 0)$  line at around  $H = 2$ . The diffuse scattering is seen to decrease with increasing temperature. The fitted integrated amplitude  $S$  of the peak is shown in Fig. 4(b) and follows a similar decrease as was seen for the peaks in the 3D-m $\Delta$ PDF in Fig. 3(e). The average correlation length is found to be 17.3(6) Å at 7 K and is approximately constant within the error bars over the whole temperature range, as shown in Fig. 4(c). This is in good agreement with the 3D-m $\Delta$ PDF, where features are seen up to approximately 15 Å. It is noteworthy that there is still a very weak signal left at 300 K, which gives approximately the same average correlation length as the low-temperature data, although with a much larger uncertainty. Observation of temperature-independent correlation lengths over a wide temperature range combined with a slow decay of diffuse scattering amplitudes with increasing temperature have previously been reported for other concentrated spin-glass systems [36]. In the production of the 3D-m $\Delta$ PDF, the 300-K dataset was subtracted from lower temperature data to isolate the magnetic contribution to the diffuse scattering. As we find that there still appears to be a very weak magnetic signal at 300 K, this subtraction also removes a small part of the magnetic signal. We do not expect this to have a significant influence on the resulting 3D-m $\Delta$ PDF, as it appears both from Figs. 2(a)–2(d) and Fig. 4 that only the scale of intensity of the magnetic diffuse signal changes with temperature, while the shape and relative intensity distribution around reciprocal space are independent of temperature. This would result in the isolated magnetic diffuse scattering and thereby also the 3D-m $\Delta$ PDF having a slightly lowered overall scale. The different temperatures would be

affected equally by this, thereby introducing a small constant downshift in the scale of the resulting 3D-m $\Delta$ PDFs. The amplitudes of the correlations, as interpreted from Figs. 3(c) and 3(d), might then appear to be slightly too low. However, as there is a large agreement between the temperature dependence of the 3D-m $\Delta$ PDF peak amplitudes in Fig. 3(d) and the diffuse intensity found in the total scattering data, as plotted in Fig. 4(b), there does not seem to be a significant underestimation of the 3D-m $\Delta$ PDF scales.

#### IV. DISCUSSION

It is interesting to consider why the mixed  $\text{Fe}_{1.12}\text{Mn}_{0.88}\text{O}_3$  is magnetically disordered while the pure  $\text{Mn}_2\text{O}_3$  and  $\beta\text{-Fe}_2\text{O}_3$  seem to have antiferromagnetically ordered states at low temperature. It has been shown that an fcc lattice with antiferromagnetic nearest-neighbor-only interactions will not order but that a next-nearest-neighbor interaction is needed for antiferromagnetic order [37–39]. The metal sites of the cubic bixbyite structure form a slightly distorted fcc structure and could therefore be expected to have a similar geometric frustration to the ideal fcc lattice. In the case of pure  $\text{Mn}_2\text{O}_3$ , the compound has a phase transition to an orthorhombic structure before the ordered antiferromagnetic state is obtained, thereby avoiding the geometric frustration of the fcc lattice. The addition of 9% of Fe or more fully suppresses this structural transition [24]. This could suggest that the effect of Fe is simply to keep the compound in the near-fcc structure where geometric frustration will be present. However, this simple explanation is not consistent with the reported ordered antiferromagnetic state of  $\beta\text{-Fe}_2\text{O}_3$ , which has the cubic bixbyite structure with no indication of a low temperature structural transition [28]. One explanation for this could be if the pure  $\beta\text{-Fe}_2\text{O}_3$  has stronger next-nearest-neighbor interactions than the mixed  $\text{Fe}_{1.12}\text{Mn}_{0.88}\text{O}_3$ , which would circumvent the geometric frustration of the fcc lattice. Another possibility is that  $\beta\text{-Fe}_2\text{O}_3$  does not have a long-range magnetic ordering. Although no neutron-scattering data has been reported for the compound yet, this does not seem to be the case, as heat-capacity and Mössbauer spectroscopy data are consistent with an ordered state [28,29]. A more likely explanation for the observed magnetic disorder in  $\text{Fe}_{1.12}\text{Mn}_{0.88}\text{O}_3$  might then be that it is not purely a geometrical frustration but due, either partly or fully, to the disordered distribution of  $\text{Mn}^{3+}$  and  $\text{Fe}^{3+}$  magnetic moments. Since the atomic structure of the bixbyite crystal is disordered with Mn/Fe distribution over two metal sites, it would be expected that the local magnetic structure is different depending on the local distribution of the two elements. As  $\text{Mn}^{3+}$  and  $\text{Fe}^{3+}$  have different magnetic moments, there will be differences in the Mn-Mn, Fe-Fe and Fe-Mn interactions. Furthermore, there could be differences even within each of these interaction types depending on what elements are locally surrounding a given metal center. Each metal site can be seen as having 12 first neighbors in the distorted fcc structure of only the metal atoms. A Mn-Mn interaction can vary depending on whether the Mn has only Mn neighbors or if it has 11 Fe neighbors and only 1 Mn neighbor, and so on. On top of this, the distortion of the structure gives slightly different angles and distances between neighbors, which might also depend on local elemental distribution, and this could further change the local interactions. The local spin distribution is therefore

expected to be incredibly complex in bixbyite. However, from the 3D-m $\Delta$ PDF we get a detailed 3D view of the magnetic short-range correlations, directly giving information about the preferred relative orientations of spins. This clearly shows that the short-range order is dominated by antiferromagnetic interactions between the nearest neighbors which propagate through the structure, giving alternating signs for the correlations depending on the order of the neighbor.

From the 3D-m $\Delta$ PDF it is seen that the magnetic correlations of the low-temperature state are present well above the 32-K peak in the magnetization data, showing the buildup of local correlations to occur over a wide temperature range. These results are in good agreement with the physical property measurements, where a deviation from ideal paramagnetic Curie-Weiss behavior is apparent already below 150 K, and no clear peak is found in the heat-capacity measurement at 32 K, as was shown in [18]. It is common for spin-glass systems to have strong local correlations at temperatures up to around 5 times the transition temperature given by the peak in magnetization data [36,40–45]. Here we see that very weak local correlations are present even at 10 times the transition temperature. The peak in magnetization data shows the temperature at which the spins freeze into a static configuration, or at least have slower dynamics than the timescale of the measurement. Above the transition, the same local correlations will be present but will not be frozen in time. This also means that the diffuse scattering above the spin-glass transition is not strictly elastic but quasielastic. However, the energy discrimination of the CORELLI instrument used for these experiments includes both the elastic and quasielastic signal, allowing us to see the correlation both below and above the spin-glass transition.

The physical property measurements showed a negative Weiss temperature, indicating antiferromagnetic interactions in the paramagnetic regime. This agrees with the low-temperature magnetic correlations in the glassy state found from the 3D-m $\Delta$ PDF. The correlation length has been estimated from two different approaches, giving results in good agreement. One is by the length for which features are seen in the 3D-m $\Delta$ PDF, which is up to around 15 Å. The other is by analyzing the broadness of the diffuse scattering features, giving a result of 17.3(6) Å at 7 K. The consistency of these methods should be expected, as the 3D-m $\Delta$ PDF contains the same information as the diffuse scattering but in a format which is more intuitive to interpret.

In conclusion, we have followed the structure, properties, and short-range magnetic correlations over a wide temperature range for bixbyite mineral samples with overall composition  $\text{Fe}_{1.12}\text{Mn}_{0.88}\text{O}_3$ . The Fe and Mn atoms are disordered over the two metal sites, with Fe having a preference for the more symmetric *8b* site, in agreement with earlier Mössbauer studies. Upon cooling, bixbyite undergoes a spin-glass transition near 32 K with no change in the atomic structure. The magnetic correlations of the spin-glass state are found to be present to much higher temperatures than the glass transition temperature, consistent with other spin-glass systems [36,40–45]. The magnetism is dominated by antiferromagnetic interactions between nearest metal sites, which propagate to give correlations that are observed up to distances

of 15 Å. The average correlation length is found to be independent of temperature, while the correlation strength decreases with increasing temperature over a wide temperature range, which are features that have previously been found for other concentrated spin-glass systems [36]. Bixbyite presents a complex, atomically disordered system where conventional methods for studying short-range order are severely challenged. However, with use of the 3D-m $\Delta$ PDF the average magnetic correlations can be established, as it provides a model-independent real-space view of magnetic correlations. Through this approach, we have revealed that the local magnetism is dominated by antiferromagnetic interactions, but

long-range order is inhibited by the atomic disorder that disrupts these correlations.

### ACKNOWLEDGMENTS

Kasper Tolborg is thanked for fruitful discussions. A portion of this research used resources at the Spallation Neutron Source, a DOE Office of Science User Facility operated by the Oak Ridge National Laboratory. Physical property characterization (AFM) was supported by the US Department of Energy, Office of Science, Basic Energy Sciences, Materials Sciences and Engineering Division. The work was supported by the Danish National Research Foundation (DNRF93).

- 
- [1] A. Banerjee, C. A. Bridges, J. Yan, A. A. Aczel, L. Li, M. B. Stone, G. E. Granroth, M. D. Lumsden, Y. Yiu, J. Knolle *et al.*, Proximate Kitaev quantum spin liquid behaviour in a honeycomb magnet, *Nat. Mater.* **15**, 733 (2016).
- [2] A. Banerjee, J. Yan, J. Knolle, C. A. Bridges, M. B. Stone, M. D. Lumsden, D. G. Mandrus, D. A. Tennant, R. Moessner, and S. E. Nagler, Neutron scattering in the proximate quantum spin liquid  $\alpha$ - $\text{RuCl}_3$ , *Science* **356**, 1055 (2017).
- [3] D. J. P. Morris, D. A. Tennant, S. A. Grigera, B. Klemke, C. Castelnovo, R. Moessner, C. Czternasty, M. Meissner, K. C. Rule, J. U. Hoffmann *et al.*, Dirac Strings and magnetic monopoles in the spin ice  $\text{Dy}_2\text{Ti}_2\text{O}_7$ , *Science* **326**, 411 (2009).
- [4] T. Fennell, P. P. Deen, A. R. Wildes, K. Schmalzl, D. Prabhakaran, A. T. Boothroyd, R. J. Aldus, D. F. McMorrow, and S. T. Bramwell, Magnetic Coulomb phase in the spin ice  $\text{Ho}_2\text{Ti}_2\text{O}_7$ , *Science* **326**, 415 (2009).
- [5] J. A. M. Paddison, H. S. Ong, J. O. Hamp, P. Mukherjee, X. Bai, M. G. Tucker, N. P. Butch, C. Castelnovo, M. Mourigal, and S. E. Dutton, Emergent order in the kagome Ising magnet  $\text{Dy}_3\text{Mg}_2\text{Sb}_3\text{O}_{14}$ , *Nat. Commun.* **7**, 13842 (2016).
- [6] S. H. Lee, C. Broholm, W. Ratcliff, G. Gasparovic, Q. Huang, T. H. Kim, and S. W. Cheong, Emergent excitations in a geometrically frustrated magnet, *Nature (London)* **418**, 856 (2002).
- [7] S. H. Lee, C. Broholm, G. Aeppli, A. P. Ramirez, T. G. Perring, C. J. Carlile, M. Adams, T. J. L. Jones, and B. Hessen, Spin-glass and non-spin-glass features of a geometrically frustrated magnet, *Europhys. Lett.* **35**, 127 (1996).
- [8] S. V. Kalinin, Multiferroics: Making a point of control, *Nat. Phys.* **13**, 115 (2017).
- [9] B.-K. Jang, J. H. Lee, K. Chu, P. Sharma, G.-Y. Kim, K.-T. Ko, K. E. Kim, Y.-J. Kim, K. Kang, H.-B. Jang *et al.*, Electric-field-induced spin disorder-to-order transition near a multiferroic triple phase point, *Nat. Phys.* **13**, 189 (2017).
- [10] H. D. Zhou, J. Lu, R. Vasic, B. W. Vogt, J. A. Janik, J. S. Brooks, and C. R. Wiebe, Relief of frustration through spin disorder in multiferroic  $\text{Ho}_{1-x}\text{Y}_x\text{MnO}_3$ , *Phys. Rev.* **B75**, 132406 (2007).
- [11] J. K. Glasbrenner, I. I. Mazin, H. O. Jeschke, P. J. Hirschfeld, R. M. Fernandes, and R. Valenti, Effect of magnetic frustration on nematicity and superconductivity in iron chalcogenides, *Nat. Phys.* **11**, 953 (2015).
- [12] J. M. Tranquada, J. D. Axe, N. Ichikawa, Y. Nakamura, S. Uchida, and B. Nachumi, Neutron-scattering study of stripe-phase order of holes and spins in  $\text{La}_{1.48}\text{Nd}_{0.4}\text{Sr}_{0.12}\text{CuO}_4$ , *Phys. Rev. B* **54**, 7489 (1996).
- [13] P. Manuel, L. C. Chapon, P. G. Radaelli, H. Zheng, and J. F. Mitchell, Magnetic Correlations in the Extended Kagome  $\text{YBaCo}_4\text{O}_7$  Probed by Single-Crystal Neutron Scattering, *Phys. Rev. Lett.* **103**, 037202 (2009).
- [14] J. A. M. Paddison, M. J. Gutmann, J. R. Stewart, M. G. Tucker, M. T. Dove, D. A. Keen, and A. L. Goodwin, Magnetic structure of paramagnetic MnO, *Phys. Rev. B* **97**, 014429 (2018).
- [15] J. A. M. Paddison, J. R. Stewart, and A. L. Goodwin, SPINVERT: A program for refinement of paramagnetic diffuse scattering data, *J. Phys.: Condens. Matter.* **25**, 454220 (2013).
- [16] B. A. Frandsen, X. H. Yang, and S. J. L. Billinge, Magnetic pair distribution function analysis of local magnetic correlations, *Acta Crystallogr., Sect. A* **70**, 3 (2014).
- [17] B. A. Frandsen and S. J. L. Billinge, Magnetic structure determination from the magnetic pair distribution function (mPDF): ground state of MnO, *Acta Crystallogr., Sect. A* **71**, 325 (2015).
- [18] N. Roth, A. F. May, F. Ye, B. C. Chakoumakos, and B. B. Iversen, Model-free reconstruction of magnetic correlations in frustrated magnets, *IUCrJ* **5**, 410 (2018).
- [19] S. Erokhin, D. Berkov, and A. Michels, Dipolar spin-misalignment correlations in inhomogeneous magnets: Comparison between neutron scattering and micromagnetic approaches, *Phys. Rev. B* **92**, 014427 (2015).
- [20] D. Mettus and A. Michels, Small-angle neutron scattering correlation functions of bulk magnetic materials, *J. Appl. Crystallogr.* **48**, 1437 (2015).
- [21] L. Pauling and M. D. Shappell, The crystal structure of bixbyite and the C-modification of the sesquioxides, *Z. Kristallogr.* **75**, 128 (1930).
- [22] E. Banks, E. Kostiner, and G. K. Wertheim, Mössbauer effect in  $\text{MnFeO}_3$ , *J. Chem. Phys.* **45**, 1189 (1966).
- [23] R. R. Chevalier, G. Rault, and E. F. Bertaut, Etude par effet Mossbauer du systeme  $\text{Mn}_{2-x}\text{Fe}_x\text{O}_3$  et transitions magnetiques dans  $\text{Mn}_2\text{O}_3$  par diffraction neutronique, *Solid State Commun.* **5**, 7 (1967).
- [24] R. W. Grant, S. Geller, J. A. Cape, and G. P. Espinosa, Magnetic and crystallographic transitions in the  $\alpha$ - $\text{Mn}_2\text{O}_3$ - $\text{Fe}_2\text{O}_3$  system, *Phys. Rev.* **175**, 686 (1968).
- [25] J. Nell, H. Pollak, and J. A. Lodya, Intersite cation partitioning in natural and synthetic  $\alpha$ -(Fe, Mn) $_2\text{O}_3$  (bixbyite)

- solid solutions determined from  $^{57}\text{Fe}$  Mossbauer spectroscopy, *Hyperfine Interact.* **91**, 601 (1994).
- [26] E. Cockayne, I. Levin, H. Wu, and A. Llobet, Magnetic structure of bixbyite  $\alpha\text{-Mn}_2\text{O}_3$ : A combined DFT+U and neutron diffraction study, *Phys. Rev. B* **87**, 184413 (2013).
- [27] T. Danno, D. Nakatsuka, Y. Kusano, H. Asaoka, M. Nakanishi, T. Fujii, Y. Ikeda, and J. Takada, Crystal structure of  $\beta\text{-Fe}_2\text{O}_3$  and topotactic phase transformation to  $\alpha\text{-Fe}_2\text{O}_3$ , *Cryst. Growth Des.* **13**, 770 (2013).
- [28] O. Malina, J. Tuček, P. Jakubec, J. Kašík, I. Medřík, H. Tokoro, M. Yoshikiyo, A. Namai, S. Ohkoshih, and R. Zbořil, Magnetic ground state of nanosized beta- $\text{Fe}_2\text{O}_3$  and its remarkable electronic features, *RSC Adv.* **5**, 49719 (2015).
- [29] Y. Ikeda, M. Takano, and Y. Bando, Formation mechanism of needle-like  $\alpha\text{-Fe}_2\text{O}_3$  particles grown along the c axis and characterization of precursorily formed  $\beta\text{-Fe}_2\text{O}_3$ , *Bull. Inst. Chem. Res., Kyoto Univ.* **64**, 249, (1986).
- [30] S. Rosenkranz and R. Osborn, Corelli: Efficient single crystal diffraction with elastic discrimination, *Pramana-J. Phys.* **71**, 705 (2008).
- [31] F. Ye, Y. Liu, R. Whitfield, R. Osborn, and S. Rosenkranz, Implementation of cross correlation for energy discrimination on the time-of-flight spectrometer CORELLI, *J. Appl. Crystallogr.* **51**, 315 (2018).
- [32] G. M. Sheldrick, XPREP, Bruker-AXS, Madison, Wisconsin, USA, 2001.
- [33] G. M. Sheldrick, A short history of SHELX, *Acta Crystallogr., Sect. A* **64**, 112 (2008).
- [34] J. Rodríguez-Carvajal, Recent advances in magnetic structure determination by neutron powder diffraction, *Phys. B: Condens. Matter* **192**, 55 (1993).
- [35] E. Christiansen, J. V. Bikun, M. Sheridan, and D. Burt, Geochemical evolution of topaz rhyolites from the Thomas Range and Spor Mountain, Utah, *Am. Mineral.* **69**, 223 (1984).
- [36] K. Motoya and Y. Muraoka, Neutron scattering study of concentrated spin glass alloys  $\text{Fe}_{65}(\text{Ni}_{1-x}\text{Mn}_x)_{35}$ , *J. Phys. Soc. Jpn* **62**, 2819 (1993).
- [37] P. W. Anderson, Generalizations of the Weiss molecular field theory of antiferromagnetism, *Phys. Rev.* **79**, 705 (1950).
- [38] Y.-Y. Li, Application of the Bethe-Weiss method to the theory of antiferromagnetism, *Phys. Rev.* **84**, 721 (1951).
- [39] M. E. Lines, Antiferromagnetism in the face-centered cubic lattice. I. The random-phase Green's function approximation, *Phys. Rev.* **139**, A1304 (1965).
- [40] K. Binder and A. P. Young, Spin glasses: Experimental facts, theoretical concepts, and open questions, *Rev. Mod. Phys.* **58**, 801 (1986).
- [41] A. F. J. Morgownik and J. A. Mydosh, Analysis of the high-temperature spin-glass susceptibility: Determination of the local magnetic exchange, *Solid State Commun.* **47**, 321 (1983).
- [42] K. V. Rao, M. Fähnle, E. Figueroa, O. Beckman, and L. Hedman, Deviations from Curie-Weiss behavior in spin-glasses, *Phys. Rev. B* **27**, 3104 (1983).
- [43] U. Köbler and K. Binder, Paramagnetic susceptibility of  $\text{Eu}_x\text{Sr}_{1-x}\text{S}$ : Experiment and comparison with high-temperature series expansion, *J. Mag. Mag. Mater.* **15-18**, 313 (1980).
- [44] G. Ehlers, J. E. Greedan, J. R. Stewart, K. C. Rule, P. Fouquet, A. L. Cornelius, C. Adriano, P. G. Pagliuso, Y. Qiu, and J. S. Gardner, High resolution neutron scattering study of  $\text{Tb}_2\text{Mo}_2\text{O}_7$ : A geometrically frustrated spin glass, *Phys. Rev. B* **81**, 224405 (2010).
- [45] A. P. Murani, Neutron scattering studies of spin-glass alloys, *J. Appl. Phys.* **49**, 1604 (1978).